

Final Report for CRESCENT Award 2017Y0SD

**Synergizing megathrust Seismo-Geodetic coupling and slip models
using Optimal Transport and Machine Learning Frameworks to
mitigate earthquake hazard in Cascadia**

Investigators:

Bar Oryan (UCSD)
Alice-Agnes Gabriel (UCSD)

Budget and Project Period of Performance:
May 1, 2024 through April 30, 2025

Budget:
\$30,000 (= 2.5 months of effort for PostDoc Bar Oryan)



A. Motivation and overview

Geodesists routinely measure interseismic surface displacements and invert them to estimate the distribution of slip deficit (also known as coupling models) along subduction interfaces (1–4). These geodetic coupling models are commonly used to assess seismic hazard, particularly in regions where historical earthquake records are sparse, such as the Cascadia subduction zone (5, 6) with the assumption that future megathrust events are more likely to rupture geodetically locked sections of the interface.

One limitation of this approach is that it relies on surface displacement data measured over just a few decades, which represents only a small fraction of the timescales over which earthquake cycles operate, typically hundreds to thousands of years. This is echoed by recent geodetic observations showing that the state of coupling along subduction megathrusts can change over surprisingly short periods, sometimes within just a few years (7–10). Furthermore, recent laboratory measurements and numerical modeling of earthquake cycles indicate that the relationship between fault locking degree and capacity to host earthquakes is more complex than previously thought (11–13).

Our project initiated the development of a framework that integrates geodetic coupling models from multiple subduction zones into a unified fault model, extending the observational record from a few decades at each location to several centuries. This framework enables the projection of coseismic slip from regions with well-documented earthquakes onto places like Cascadia, where finite slip models are absent, eventually allowing us to evaluate the seismic risk more precisely. To accomplish this, we follow a three-stage approach. First, we compile and unify all available geodetic coupling and finite slip models from megathrusts worldwide. Second, we systematically evaluate whether and how coupling and coseismic slip are correlated using the full set of available seismic data. Third, we train a neural network that maps source coupling distributions from Japan (3) and Chile (14) onto a target Cascadia megathrust coupling (15). This mapping preserves the inherent geodetic characteristics of the coupling models and is used to project finite slip distributions from Chile and Japan onto the target region.

B. Results

1. *Compilation of megathrusts geodetic coupling and finite slip models*

We gathered coupling models for **fourteen subduction zones**, prioritizing coupling models that incorporate the most current geodetic observations (Fig. 1). In addition to the coupling data, we collected **57 finite slip models** corresponding to earthquakes along the same fourteen active margins. About a third of our finite slip models were obtained from Hayes (2017), who used consistent inversions of body and surface waves, compiling finite slip models for over 160 earthquakes.

We used USGS finite fault solutions (16–40) for recent earthquakes not covered by Hayes (41). Lastly, we supplemented our dataset with historic slip models from other published studies (42–51). Together, our compiled dataset spans a century of megathrust earthquakes (Fig. 2), from the 1923 Kanto earthquake (52) to a magnitude 7.0 event that ruptured the Kamchatka megathrust in August 2024 (28).

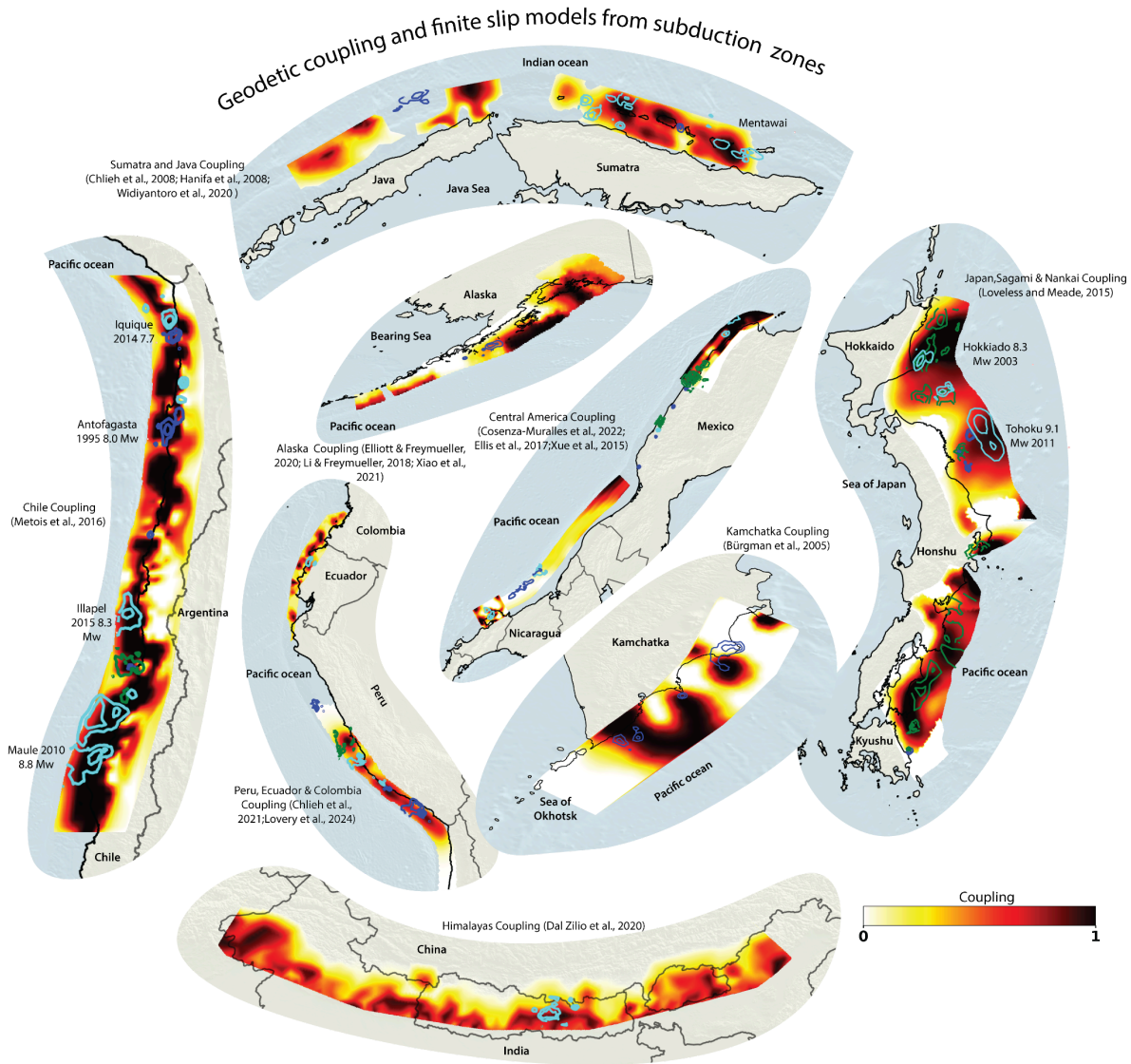


Fig 1 - Coupling distributions for fourteen active margins (1, 3, 14, 53–61) and 57 finite slip models. Blue, cyan, and green contours indicate finite slip models computed by USGS (16–40), Hayes (41) and other workers (42–51), respectively. Solutions were obtained from SRCMOD database (62).

2. Comparison between geodetic coupling and slip model

Although not part of our original plan, we realized that the neural network relies on the relationship between interseismic coupling and coseismic slip, prompting us to systematically evaluate this correlation. Previous work explored primarily individual subduction zones and only large megathrust earthquakes (2, 14, 63–65).

We use our global dataset (Fig. 1) to quantify this correlation and convert each finite-slip model into a probability density function (PDF). Consequently, we sample the PDF into a discrete cloud of points, such that a higher point density represents regions of larger slip. We extract the corresponding coupling value for each sampled point, allowing us to characterize the relationship between slip and coupling by constructing cumulative distribution functions (CDFs) of the extracted coupling values. We demonstrate that larger earthquakes tend to exhibit a stronger correlation with highly coupled regions. For instance, only ~10% of the slip for events smaller than moment magnitude 7.5 occur in areas where the coupling value is 1.0. In contrast, for the full set of events,

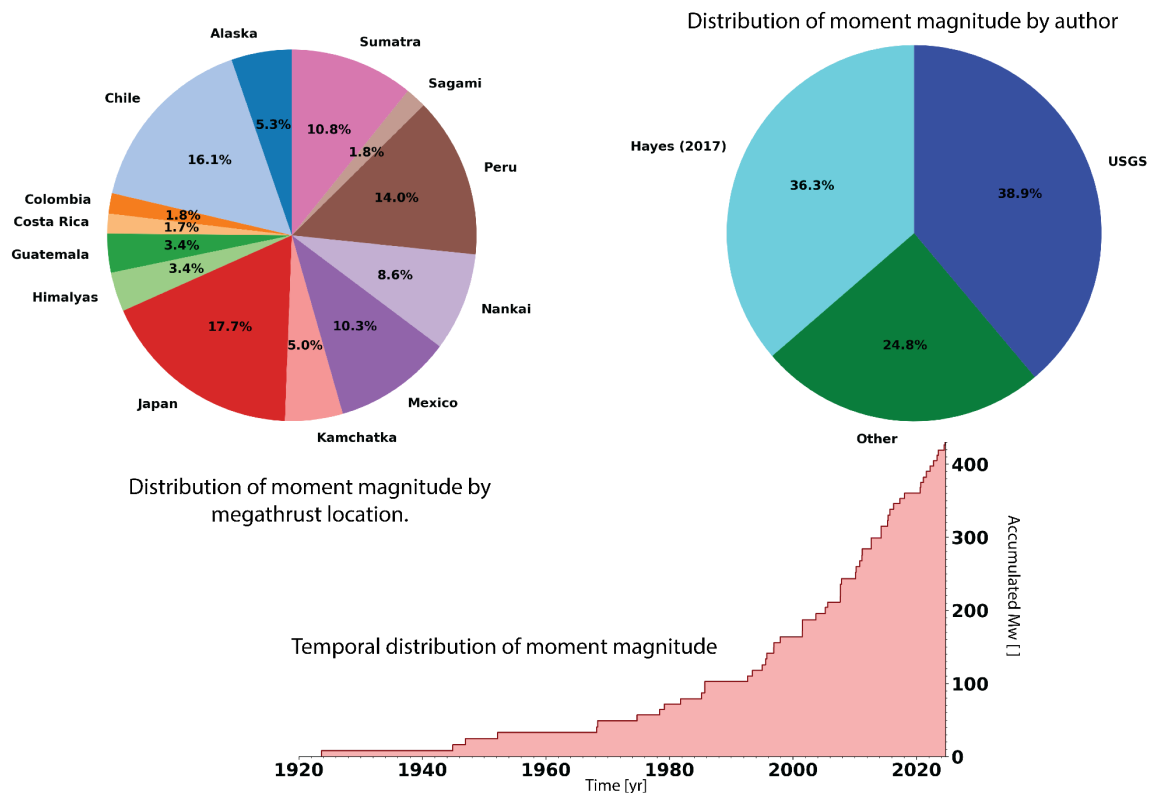


Fig 2 - Source, spatial and temporal distributions of moment magnitude for the obtained finite slip models(16–39, 41–51).

approximately 25% of the total slip is concentrated in these highly coupled regions (Fig. 3A). We also find that most subduction zones exhibit a broadly similar correlation between slip and coupling. Among them, Chilean earthquakes show the strongest correlation, while Guatemala displays the weakest, though the latter is likely an outlier (Fig. 3B).

Lastly, we evaluate the observed correlation in the context of theoretical expectations, and compare our results with synthetic earthquake cycles generated using simulations of sequences of earthquakes and aseismic slip (SEAS) implemented in the open-source code tandem (66). While the relationship between geodetic coupling and slip may vary across fault systems due to differences in geometry and frictional properties, we adopt parameters representative of central Cascadia to capture first-order correlations under realistic tectonic settings. To this end, we simulate a 10° shallowly dipping megathrust governed by aging-law rate-and-state friction in 2D (Fig. 3C). We show that the observed correlation is weaker than the patterns predicted by our idealized rate-and-state-based simulation (Fig. 3A), which may suggest an important role of along-dip or along-strike stress and strength heterogeneities.

We note that the sampling approach presented here was initially developed to convert finite-slip models into point-based data for our neural network (Section 3), which operates exclusively on discrete spatial inputs. However, we found that this discretization also provides an effective statistical framework for assessing the spatial correlation between coupling and slip across subduction zones.

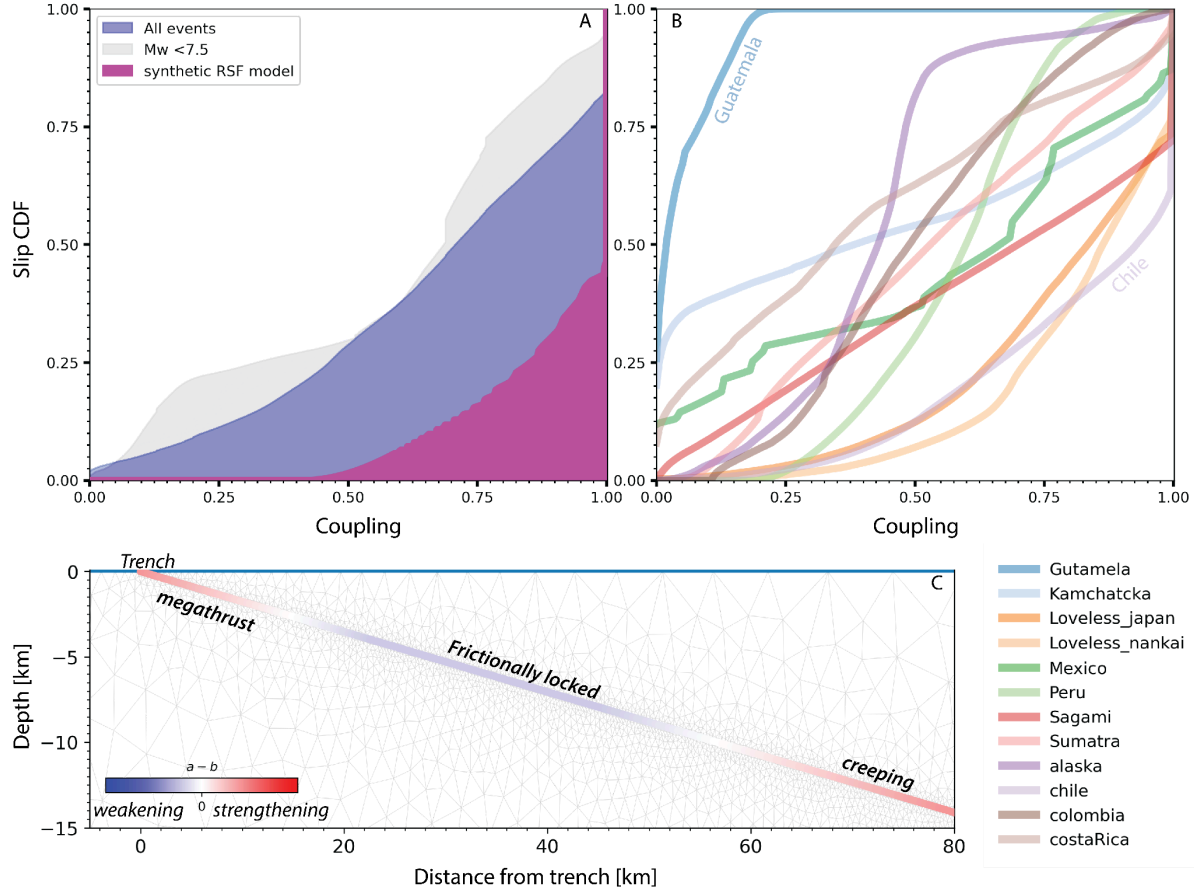


Fig 3 - Correlation between interseismic coupling and coseismic slip. A - Stacked slip–coupling cumulative distribution functions (CDF) for all finite-slip models (blue), Mw<7.5 (grey) and synthetic earthquakes (magenta) generated along a megathrust governed by rate-and-state friction (RSF). For example, the magenta and blue curves indicate that ~60% and ~25% of total slip occurs in regions with near-complete coupling (coupling ≈ 1) for synthetic and observed earthquakes, respectively. B - Stacked slip–coupling CDFs group by subduction zone. C - Model domain used to generate synthetic earthquake sequences, featuring a megathrust dipping at 10° with frictional properties selected to broadly replicate interseismic behavior observed in the central Cascadia subduction zone.

3. Synergizing megathrust Seismo-Geodetic coupling and slip models

We develop a framework that synergizes principles of optimal transport and machine learning to create a proof-of-concept seismo-geodetic Cascadia fault slip model, assimilating long-term and co-seismic geodetic-seismo observables from Chile and Japan. Our algorithm has two components, (1) the Wasserstein Generative Adversarial Networks (63) which is trained to produce projection, G , to map discrete samples, \vec{x} , from a source coupling distribution, S , to target coupling distribution, T by minimizing the Wasserstein distance $L_W = \frac{1}{N} \sum_{i=1}^N \|\vec{x}_i - G(\vec{x}_i)\|$ where N is the number of samples in the batch. At the same time, the network is trained to preserve the intrinsic geometry of the coupling distribution by minimizing pairwise distances between T and S using the following (2) $L_{\text{cons}} = \frac{1}{N^2} \sum_{i,j=1}^N \|\|\vec{x}_i - \vec{x}_j\| - \|G(\vec{x}_i) - G(\vec{x}_j)\|\|$. This formulation ensures that (1) the overall

shape of the source coupling distribution is projected into the target style (Fig 4B,C), and (2) the relative distances among sample points (linked to T and S) remain consistent, which preserves the dimensions of projection. We can then generate discrete samples using finite slip models (see section 2) and use G to move them from one subduction to another (Fig. 4A). We note that our original formulation aimed to preserve the intrinsic geometry of the coupling distribution by minimizing the difference in coupling values between the source and target domains (minimizing $C_S(\vec{x}) - C_T(G(\vec{x}))$ where $C(\vec{x})$ returns coupling value at \vec{x}). However, we observed that this formulation, when applied to real coupling models, often fails to preserve the geometric structure of the source distribution and can result in projections where earthquake rupture areas become unrealistically large while exhibiting very low slip values.

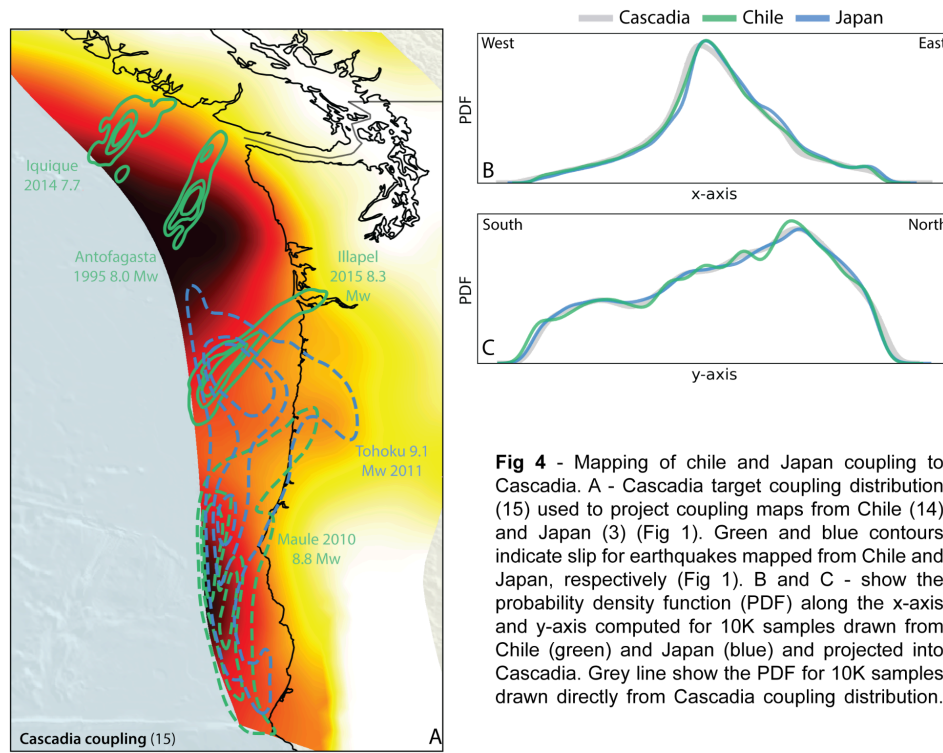


Fig 4 - Mapping of Chile and Japan coupling to Cascadia. A - Cascadia target coupling distribution (15) used to project coupling maps from Chile (14) and Japan (3) (Fig 1). Green and blue contours indicate slip for earthquakes mapped from Chile and Japan, respectively (Fig 1). B and C - show the probability density function (PDF) along the x-axis and y-axis computed for 10K samples drawn from Chile (green) and Japan (blue) and projected into Cascadia. Grey line show the PDF for 10K samples drawn directly from Cascadia coupling distribution.

C. Future steps

- Finish a first manuscript that summarizes the results of section B.2 by the end of summer 2025.
Expand our optimal transport and machine learning analysis (section B.3) to include all subduction zones beyond just Chile and Japan, and investigate whether our revised formulation performs consistently across all regions, with the goal of submitting a second manuscript in winter 2026.

D. Presentations

- Poster Presentation at the SSA Annual Meeting 2025 ([Oryan & Gabriel, SSA 2025](#))
- Invited talk, Rutgers University, Department of Earth and Planetary Sciences, March 2025.
- Invited talk, Dartmouth College, Department of Earth Science, February 2025.
- Invited talk, University of Oregon, Department of Earth Sciences, January 2025.

References

1. R. Bürgmann, M. G. Kogan, G. M. Steblov, G. Hilley, V. E. Levin, E. Apel, Interseismic coupling and asperity distribution along the Kamchatka subduction zone. *Journal of Geophysical Research: Solid Earth* **110** (2005).
2. A. O. Konca, J.-P. Avouac, A. Sladen, A. J. Meltzner, K. Sieh, P. Fang, Z. Li, J. Galetzka, J. Genrich, M. Chlieh, D. H. Natawidjaja, Y. Bock, E. J. Fielding, C. Ji, D. V. Helmberger, Partial rupture of a locked patch of the Sumatra megathrust during the 2007 earthquake sequence. *Nature* **456**, 631–635 (2008).
3. J. P. Loveless, B. J. Meade, Two decades of spatiotemporal variations in subduction zone coupling offshore Japan. *Earth and Planetary Science Letters* **436**, 19–30 (2016).
4. M. Métois, A. Socquet, C. Vigny, Interseismic coupling, segmentation and mechanical behavior of the central Chile subduction zone. *Journal of Geophysical Research: Solid Earth* **117** (2012).
5. M. D. Ramos, Y. Huang, T. Ulrich, D. Li, A.-A. Gabriel, A. M. Thomas, Assessing Margin-Wide Rupture Behaviors Along the Cascadia Megathrust With 3-D Dynamic Rupture Simulations. *Journal of Geophysical Research: Solid Earth* **126**, e2021JB022005 (2021).
6. D. T. Small, D. Melgar, Geodetic Coupling Models as Constraints on Stochastic Earthquake Ruptures: An Example Application to PTHA in Cascadia. *Journal of Geophysical Research: Solid Earth* **126**, e2020JB021149 (2021).
7. H. Luo, B. Ambrosius, R. M. Russo, V. Mocanu, K. Wang, M. Bevis, R. Fernandes, A recent increase in megathrust locking in the southernmost rupture area of the giant 1960 Chile earthquake. *Earth and Planetary Science Letters* **537**, 116200 (2020).
8. L. Marill, D. Marsan, A. Socquet, M. Radiguet, N. Cotte, B. Rousset, Fourteen-Year Acceleration Along the Japan Trench. *Journal of Geophysical Research: Solid Earth* **126**, e2020JB021226 (2021).
9. K. Materna, N. Bartlow, A. Wech, C. Williams, R. Bürgmann, Dynamically Triggered Changes of Plate Interface Coupling in Southern Cascadia. *Geophys. Res. Lett.* **46**, 12890–12899 (2019).
10. L. Maubant, W. B. Frank, L. M. Wallace, C. A. Williams, I. Hamling, Imaging the Spatiotemporal Evolution of Plate Coupling With Interferometric Radar (InSAR) in the Hikurangi Subduction Zone. *Geophysical Research Letters* **50**, e2023GL105388 (2023).
11. D. Molina-Ormazabal, J.-P. Ampuero, A. Tassara, Diverse slip behaviour of velocity-weakening fault barriers. *Nat. Geosci.*, 1–8 (2023).
12. H. Noda, N. Lapusta, Stable creeping fault segments can become destructive as a result of dynamic weakening. *Nature* **493**, 518–521 (2013).
13. V. Rubino, N. Lapusta, A. J. Rosakis, Intermittent lab earthquakes in dynamically weakening fault gouge. *Nature* **606**, 922–929 (2022).

14. M. Métois, C. Vigny, A. Socquet, Interseismic Coupling, Megathrust Earthquakes and Seismic Swarms Along the Chilean Subduction Zone (38°–18°S). *Pure Appl. Geophys.* **173**, 1431–1449 (2016).
15. E. O. Lindsey, R. Mallick, J. A. Hubbard, K. E. Bradley, R. V. Almeida, J. D. P. Moore, R. Bürgmann, E. M. Hill, Slip rate deficit and earthquake potential on shallow megathrusts. *Nat. Geosci.* **14**, 321–326 (2021).
16. USGS, M 7.2 - 106 km S of Sand Point, Alaska.
<https://earthquake.usgs.gov/earthquakes/eventpage/us7000kg30/finite-fault>.
17. USGS, M 7.8 - 99 km SSE of Perryville, Alaska.
<https://earthquake.usgs.gov/earthquakes/eventpage/us7000asvb/finite-fault>.
18. USGS, M 8.2 - Alaska Peninsula.
<https://earthquake.usgs.gov/earthquakes/eventpage/ak0219neiszm/finite-fault>.
19. USGS, M 6.8 - 86 km NW of Vallenar, Chile.
<https://earthquake.usgs.gov/earthquakes/eventpage/us7000bfjr/finite-fault>.
20. USGS, M 6.9 - 40 km W of Valparaíso, Chile.
<https://earthquake.usgs.gov/earthquakes/eventpage/us10008kce/finite-fault>.
21. USGS, M 7.7 - 53 km SW of Iquique, Chile.
<https://earthquake.usgs.gov/earthquakes/eventpage/usc000p27i/finite-fault>.
22. USGS, M 8.0 - 36 km NNE of Antofagasta, Chile.
<https://earthquake.usgs.gov/earthquakes/eventpage/usp000714t/finite-fault>.
23. USGS, M 7.7 - 83 km SSW of Corinto, Nicaragua.
<https://earthquake.usgs.gov/earthquakes/eventpage/usp0005ddn/finite-fault>.
24. USGS, M 7.1 - 73 km ENE of Namie, Japan.
<https://earthquake.usgs.gov/earthquakes/eventpage/us6000dher/finite-fault>.
25. USGS, M 7.2 - 66 km ESE of Ishinomaki, Japan.
<https://earthquake.usgs.gov/earthquakes/eventpage/usp000dx2/finite-fault>.
26. USGS, M 7.3 - 57 km ENE of Namie, Japan.
<https://earthquake.usgs.gov/earthquakes/eventpage/us6000h519/finite-fault>.
27. USGS, M 7.3 - 120 km SE of Funato, Japan.
<https://earthquake.usgs.gov/earthquakes/eventpage/usp000hvhj/finite-fault>.
28. USGS, M 7.0 - 102 km E of Petropavlovsk-Kamchatsky, Russia.
<https://earthquake.usgs.gov/earthquakes/eventpage/us7000n7n8/finite-fault>.
29. USGS, M 7.3 - 187 km SE of Ust'-Kamchatsk Staryy, Russia.
<https://earthquake.usgs.gov/earthquakes/eventpage/us2000ivfw/finite-fault>.
30. USGS, M 7.5 - 97 km ESE of Ozernovskiy, Russia.
<https://earthquake.usgs.gov/earthquakes/eventpage/usp0005u7b/finite-fault>.

31. USGS, M 7.8 - 156 km S of Ust'-Kamchatsk Staryy, Russia.
<https://earthquake.usgs.gov/earthquakes/eventpage/usp0008btk/finite-fault>.
32. USGS, M 7.2 - 4 km S of Pinotepa de Don Luis, Mexico.
<https://earthquake.usgs.gov/earthquakes/eventpage/us2000d3km/finite-fault>.
33. USGS, M 7.2 - 9 km ENE of Coyuquilla Norte, Mexico.
<https://earthquake.usgs.gov/earthquakes/eventpage/usb000pq41/finite-fault>.
34. USGS, M 7.4 - 9 km SE of Santa María Xadani, Mexico.
<https://earthquake.usgs.gov/earthquakes/eventpage/us6000ah9t/finite-fault>.
35. USGS, M 7.6 - 35 km SSW of Aguililla, Mexico.
<https://earthquake.usgs.gov/earthquakes/eventpage/us7000i9bw/finite-fault>.
36. USGS, M 7.1 - 37 km W of Atiquipa, Peru.
<https://earthquake.usgs.gov/earthquakes/eventpage/us2000cjfy/finite-fault>.
37. USGS, M 7.2 - 10 km WSW of Atiquipa, Peru.
<https://earthquake.usgs.gov/earthquakes/eventpage/us6000n8tq/finite-fault>.
38. USGS, M 7.6 - 51 km SW of Punta de Bombón, Peru.
<https://earthquake.usgs.gov/earthquakes/eventpage/usp000aj40/finite-fault>.
39. USGS, M 8.4 - 6 km SSW of Atico, Peru.
https://earthquake.usgs.gov/earthquakes/eventpage/official20010623203314130_33/finite-fault.
40. D. E. Goldberg, P. Koch, D. Melgar, S. Riquelme, W. L. Yeck, Beyond the Teleseism: Introducing Regional Seismic and Geodetic Data into Routine USGS Finite-Fault Modeling. *Seismological Research Letters* **93**, 3308–3323 (2022).
41. G. P. Hayes, The finite, kinematic rupture properties of great-sized earthquakes since 1990. *Earth and Planetary Science Letters* **468**, 94–100 (2017).
42. H. Kobayashi, K. Koketsu, H. Miyake, H. Kanamori, Similarities and Differences in the Rupture Processes of the 1952 and 2003 Tokachi-Oki Earthquakes. *JGR Solid Earth* **126**, e2020JB020585 (2021).
43. R. Nagai, M. Kikuchi, Y. Yamanaka, Comparative study on the source processes of recurrent large earthquakes in Sanriku-oki region : the 1968 Tokachi-oki earthquake and the 1994 Sanriku-oki earthquake. *Zisin* **54**, 267–280 (2001).
44. Y. Yamanaka, M. Kikuchi, Asperity map along the subduction zone in northeastern Japan inferred from regional seismic data. *Journal of Geophysical Research: Solid Earth* **109** (2004).
45. F. Courboux, M. A. Santoyo, J. F. Pacheco, S. K. Singh, The 14 September 1995 (M = 7.3) Copala, Mexico, earthquake: A source study using teleseismic, regional, and local data. *Bulletin of the Seismological Society of America* **87**, 999–1010 (1997).

46. C. Mendoza, Coseismic slip of two large Mexican earthquakes from teleseismic body waveforms: Implications for asperity interaction in the Michoacan Plate Boundary Segment. *Journal of Geophysical Research: Solid Earth* **98**, 8197–8210 (1993).
47. C. Mendoza, Finite-fault analysis of the 1979 March 14 Petatlan, Mexico, earthquake using teleseismic P waveforms. *Geophysical Journal International* **121**, 675–683 (1995).
48. C. Mendoza, S. H. Hartzell, Slip distribution of the 19 September 1985 Michoacan, Mexico, earthquake: Near-source and teleseismic constraints. *Bulletin of the Seismological Society of America* **79**, 655–669 (1989).
49. S. Hartzell, C. Langer, Importance of model parameterization in finite fault inversions: Application to the 1974 M 8.0 Peru Earthquake. *Journal of Geophysical Research: Solid Earth* **98**, 22123–22134 (1993).
50. C. Mendoza, S. Hartzell, T. Monfret, Wide-band analysis of the 3 March 1985 central Chile earthquake: Overall source process and rupture history. *Bulletin of the Seismological Society of America* **84**, 269–283 (1994).
51. J. Rhie, D. Dreger, R. Bürgmann, B. Romanowicz, Slip of the 2004 Sumatra–Andaman Earthquake from Joint Inversion of Long-Period Global Seismic Waveforms and gps Static Offsets. *Bulletin of the Seismological Society of America* **97**, S115–S127 (2007).
52. R. Kobayashi, K. Koketsu, Source process of the 1923 Kanto earthquake inferred from historical geodetic, teleseismic, and strong motion data. *Earth, Planets and Space* **57**, 261–270 (2005).
53. M. Chlieh, J. P. Avouac, K. Sieh, D. H. Natawidjaja, J. Galetzka, Heterogeneous coupling of the Sumatran megathrust constrained by geodetic and paleogeodetic measurements. *Journal of Geophysical Research: Solid Earth* **113** (2008).
54. M. Chlieh, C. Beauval, H. Yepes, J. Marinière, M. Saillard, L. Audin, Seismic and Aseismic Cycle of the Ecuador–Colombia Subduction Zone. *Front. Earth Sci.* **9** (2021).
55. B. Cosenza-Murallas, C. DeMets, B. Márquez-Azúa, O. Sánchez, J. Stock, E. Cabral-Cano, R. McCaffrey, GPS-derived interseismic fault locking along the Jalisco–Colima segment of the Mexico subduction zone. *Geophysical Journal International* **228**, 2174–2197 (2022).
56. L. Dal Zilio, R. Jolivet, Y. van Dinther, Segmentation of the Main Himalayan Thrust Illuminated by Bayesian Inference of Interseismic Coupling. *Geophysical Research Letters* **47**, e2019GL086424 (2020).
57. A. Ellis, C. DeMets, R. McCaffrey, P. Briole, B. Cosenza Murallas, O. Flores, M. Guzmán-Speziale, D. Hernández, V. Kostoglodov, P. LaFemina, N. Lord, C. Lasserre, H. Lyon-Caen, M. Rodriguez Maradiaga, E. Molina, J. Rivera, R. Rogers, A. Staller, B. Tikoff, GPS constraints on deformation in northern Central America from 1999 to 2017, Part 2: Block rotations and fault slip rates, fault locking and distributed deformation. *Geophysical Journal International* **218**, 729–754 (2019).
58. L. Feng, A. V. Newman, M. Protti, V. González, Y. Jiang, T. H. Dixon, Active deformation

near the Nicoya Peninsula, northwestern Costa Rica, between 1996 and 2010: Interseismic megathrust coupling. *Journal of Geophysical Research: Solid Earth* **117** (2012).

59. N. R. Hanifa, T. Sagiya, F. Kimata, J. Efendi, H. Z. Abidin, I. Meilano, Interplate coupling model off the southwestern coast of Java, Indonesia, based on continuous GPS data in 2008–2010. *Earth and Planetary Science Letters* **401**, 159–171 (2014).
60. B. Lovery, M. Chlieh, E. Norabuena, J. C. Villegas-Lanza, M. Radiguet, N. Cotte, A. Tsapong-Tsague, W. Quiroz, C. Sierra Farfán, M. Simons, J. M. Nocquet, H. Tavera, A. Socquet, Heterogeneous Locking and Earthquake Potential on the South Peru Megathrust From Dense GNSS Network. *Journal of Geophysical Research: Solid Earth* **129**, e2023JB027114 (2024).
61. S. Widiyantoro, E. Gunawan, A. Muhari, N. Rawlinson, J. Mori, N. R. Hanifa, S. Susilo, P. Supendi, H. A. Shiddiqi, A. D. Nugraha, H. E. Putra, Implications for megathrust earthquakes and tsunamis from seismic gaps south of Java Indonesia. *Sci Rep* **10**, 15274 (2020).
62. P. M. Mai, K. K. S. Thingbaijam, SRCMOD: An Online Database of Finite-Fault Rupture Models. *Seismological Research Letters* **85**, 1348–1357 (2014).
63. M. Arjovsky, S. Chintala, L. Bottou, “Wasserstein Generative Adversarial Networks” in *Proceedings of the 34th International Conference on Machine Learning* (PMLR, 2017; <https://proceedings.mlr.press/v70/arjovsky17a.html>), pp. 214–223.